iScience

CellPress
OPEN ACCESS

Article

The argonaut constructs its shell via physical self-organization and coordinated cell sensorial activity

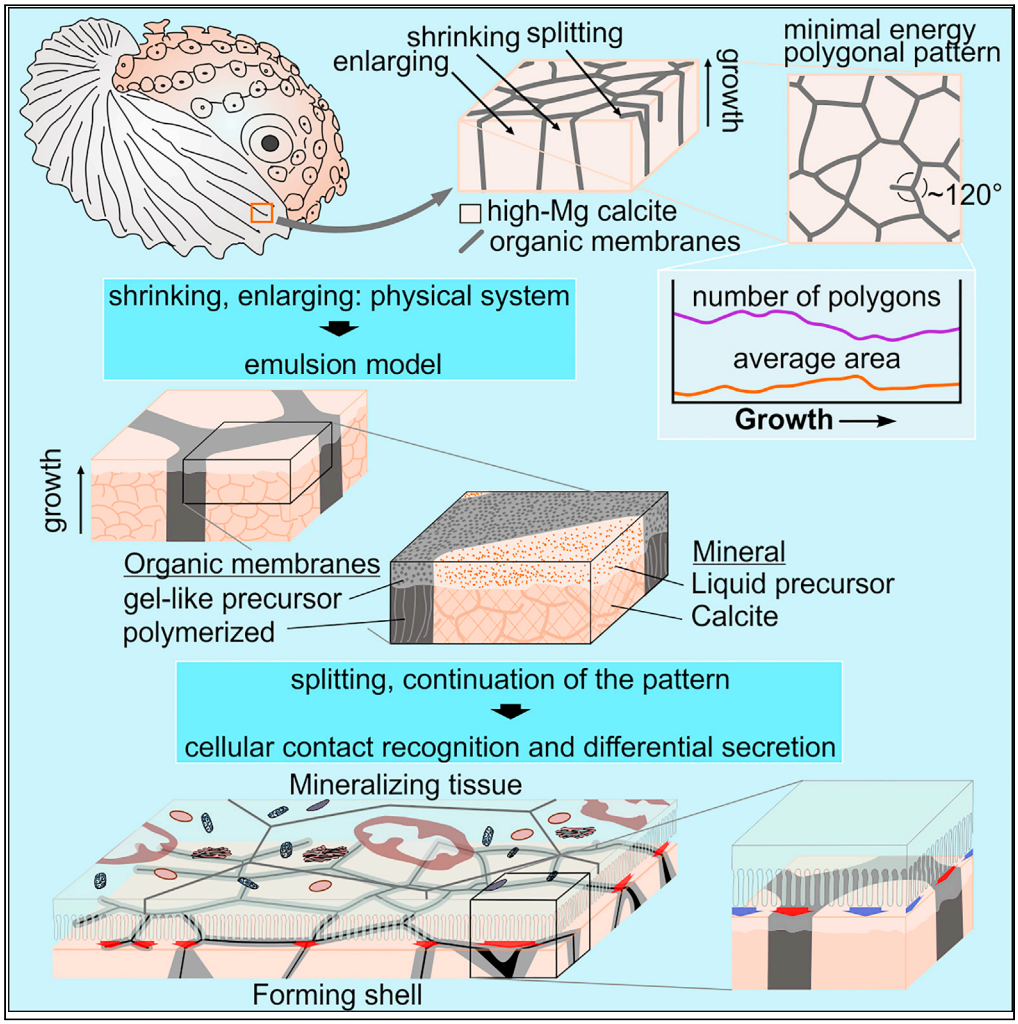

Antonio G. Checa, Fátima Linares, Christian Grenier, Erika Griesshaber, Alejandro B. Rodríguez-Navarro, Wolfgang W. Schmahl

acheca@ugr.es

Highlights

The shell consists of a polygonal organic pattern that evolves as a physical system

An emulsion model accounts for the configuration of the pattern

Mean polygon size and number is kept by the additional splitting of large polygons

Cell sensitivity explains the propagation of the pattern and polygon splitting

Checa et al., iScience *24*, 103288
November 19, 2021
https://doi.org/10.1016/j.isci.2021.103288

iScience

CellPress
OPEN ACCESS

Article

The argonaut constructs its shell via physical self-organization and coordinated cell sensorial activity

Antonio G. Checa,[1,2,6,*] Fátima Linares,[3] Christian Grenier,[1] Erika Griesshaber,[4] Alejandro B. Rodríguez-Navarro,[5] and Wolfgang W. Schmahl[4]

SUMMARY

The shell of the cephalopod *Argonauta* consists of two layers of fibers that elongate perpendicular to the shell surfaces. Fibers have a high-Mg calcitic core sheathed by thin organic membranes (>100 nm) and configurate a polygonal network in cross section. Their evolution has been studied by serial sectioning with electron microscopy-associated techniques. During growth, fibers with small cross-sectional areas shrink, whereas those with large sections widen. It is proposed that fibers evolve as an emulsion between the fluid precursors of both the mineral and organic phases. When polygons reach big cross-sectional areas, they become subdivided by new membranes. To explain both the continuation of the pattern and the subdivision process, the living cells from the mineralizing tissue must perform contact recognition of the previously formed pattern and subsequent secretion at sub-micron scale. Accordingly, the fabrication of the argonaut shell proceeds by physical self-organization together with direct cellular activity.

INTRODUCTION

The shells of proto- and metazoans are organomineral biocomposites consisting of recurrent arrangements of crystals and organic matrices, called microstructures (sometimes referred to as "structures" or "textures") (e.g., Carter et al., 2012). Microstructures are adapted for their mainly protective function, although they also provide structural support for the soft parts, prevent dissolution, help in locomotion, etc. Their impressive biomechanical properties make them highly valued scientific objects for study. Accordingly, there is strong interest in knowing the strategies used by organisms for the production of microstructures to get inspiration for the fabrication of similar highly functional synthetic products.

Except for siliceous sponges, linguliformean phosphatic brachiopods, and chordates, metazoan skeletons are based on calcium carbonate (Lowenstam and Weiner, 1989). The different taxa also have different abilities for the production of microstructures (Checa, 2018). Mollusks are, by far, the leaders in both the variety and sophistication of their microstructures. They are able to produce some twelve basic microstructures with either aragonite or calcite. Both polymorphs can be present in a single shell, where the calcite layers, if any, are always external (Bøggild, 1930). Taxa such as brachiopods (Simonet Roda et al., 2021), bryozoans (Taylor et al., 2015), and polychaetes (Vinn, 2020) are also able to produce each a moderate suite of microstructures, sometimes with only a single mineral (e.g., calcite in articulate brachiopods). Corals (Stolarski, 2003) and cirripeds (Bourget, 1987) can only secrete one or two monomineralic microstructural types.

From a strict proteomic approach, proteins are responsible for every aspect of microstructures (Heywood, 1994). Studies show that soluble proteins control the mineral phase (aragonite, calcite) (Belcher et al., 1996; Falini et al., 1996), as well as nucleation and crystal shape (Marin, 2020). But some aspects of microstructures cannot be produced by the biomolecular toolkit directly. For example, some prismatic layers of mollusks consist of calcitic or aragonitic prisms surrounded by relatively thick organic membranes (Griesshaber et al., 2018). Nacre is made of an alternation of lamellae of tablets and thin organic membranes. These and other examples have been alternatively and successfully explained by self-organization: emulsification in the prismatic layers (Checa et al., 2016a) and layer-by-layer liquid crystallization in nacre (e.g., Cartwright and Checa, 2007), sometimes coupled with a particularly sophisticated activity of the mantle cells

[1]Departamento de Estratigrafía y Paleontología, Universidad de Granada, 18071 Granada, Spain

[2]Instituto Andaluz de Ciencias de la Tierra, CSIC-Universidad de Granada, 18100 Armilla, Spain

[3]Centro de Instrumentación Científica, Universidad de Granada, 18071 Granada, Spain

[4]Department für Geo- und Umweltwissenschaften, Ludwig-Maximilians-Universität München, 80333 München, Germany

[5]Departamento de Mineralogía y Petrología, Universidad de Granada, 18071 Granada, Spain

[6]Lead contact

*Correspondence: acheca@ugr.es

https://doi.org/10.1016/j.isci.2021.103288

(e.g., substrate recognition, differential secretion, communication) (Checa et al., 2016a, 2016b). In other words, mantle cell capabilities may promote or hinder the production of microstructures. The fact that each group is characterized by a particular mantle cell structure explains the differential abilities of metazoan groups with regard to the fabrication of microstructures.

Within mollusks, cephalopods are a rather restricted group in terms of diversity (830 accepted extant species), fourth after gastropods (70,744), bivalves (9,731), and Polyplacophora (1,046) (WoRMS Editorial Board, 2021, accessed 2021-09-07). Since the demise of the ammonoids at the Cretaceous-Paleogene boundary, their diversity is based on the subclass Coleoidea, i.e., cephalopods with internal or absent shells. Presently, *Nautilus* is the only cephalopod with an external shell, and *Spirula* and *Sepia* produce internal calcified shells. The only other shell producer is the pelagic octopod genus *Argonauta*. This is a cosmopolitan genus comprising four species (Finn, 2013; WoRMS Editorial Board, 2021, accessed 2021-09-07). The female *Argonauta* (also called paper nautilus) secretes a thin spirally coiled shell, made entirely of calcite. The minute male is devoid of any shell. The first detailed observations on the secretion of the shell by the animal were made by Jeanne Villepreux-Power in the 19th century. In her (sometimes overlooked) pioneering study on *Argonauta argo* (Power, 1856), she described how the female argonaut shell is secreted by very wide membranaceous distal extensions (webs) of the two dorsal arms, and not by the mantle, as in all mollusks. This observation was confirmed by later authors (Finn, 2013; Milner, 1935; Mitchell et al., 1994; Woodward, 1880). Details about how shell growth by the webs proceeds are still lacking (Oudot et al., 2020). Accordingly, this shell is not homologous to the mollusk shell but an autapomorphy of *Argonauta*. As might be anticipated, the shell of *Argonauta* is also unique in its general structure, and microstructure. Unlike the *Nautilus* shell, the female argonaut shell is devoid of septa, siphuncle, or any other internal structure, including attachment sites of the soft parts (Adams and Adams, 1858; Power, 1856; Woodward, 1880). It is used by the female to both brood the eggs (egg-case) and trap air inside for buoyancy purposes.

The first observations of the microstructure of the shell of *Argonauta* were done with optical microscopy by Bøggild (1930), who observed that the shell consists of two finely prismatic layers, which meet at a central dark layer. Later, with the employment of electron microscopy, Kobayashi (1971) confirmed Bøggild's observations, revealed the organic nature of the central layer, and provided accurate details regarding the fibers making up the prismatic layers. Their diameters are less than one micron and consist of a calcitic core and an envelope of "reticulated" organic membranes. Later authors (Bandel and Dullo, 1984; Wolfe et al., 2012, 2013) overlooked Kobayashi's model and concentrated on the calcitic phase of the fibrous bidirectional microstructure. Only Mitchell et al. (1994) showed interesting details regarding the organic network surrounding the calcitic fibers, which they qualified as polygonal, typical of minimal surface energy configuration.

We have carried out an in-depth study of the microstructure of the shell of *Argonauta* using high-resolution microscopy techniques. We focused particularly on the evolution of the organomineral complex during growth and considered if it can be explained by means of self-organization, cell activity, or any other phenomenon. The fact that the *Argonauta* shell is secreted by an organ different from the mantle might lead one to think that it must be a rudimentary construct. We found quite the contrary. Its constructional route is extremely sophisticated, similar, or even more sophisticated than those followed by other mollusks to produce similarly complex mantle-made materials.

RESULTS

Mineralogy and composition

X-ray diffraction (XRD) analysis indicates that calcite is the only mineral phase present. The results of the Rietveld analysis (Table S1) show well-defined changes in calcite unit cell parameters with respect to pure inorganic calcite, which can be explained by both the substitution of Ca^{2+} by Mg^{2+} ions and the incorporation of organic molecules into the calcite crystal structure (Pokroy et al., 2006). In particular, the reduction in calcite unit cell parameters observed in the sample treated at 400°C ($\Delta a = -0.0432 \pm 3 \times 10^{-4}$ Å = −0.865%; $\Delta c = -0.19678 \pm 9 \times 10^{-4}$ Å = −1.153%), when the influence of organic matter is negligible, can be explained by a 10.4% (molar) substitution of Ca^{2+} by smaller Mg^{2+} ions (Dos Santos et al., 2017). The expansion of calcite unit cell parameters (Δa = 0.107%, and Δc = 0.082%) observed in the untreated shell mineral compared with the sample treated at 400°C (no organic matter) may result from the incorporation of organic shell components into the calcite crystal structure.

The amount of amorphous material estimated by XRD using silicon as an internal standard was 6.88% by weight. On the other hand, thermogravimetry analysis coupled with differential scanning calorimetry

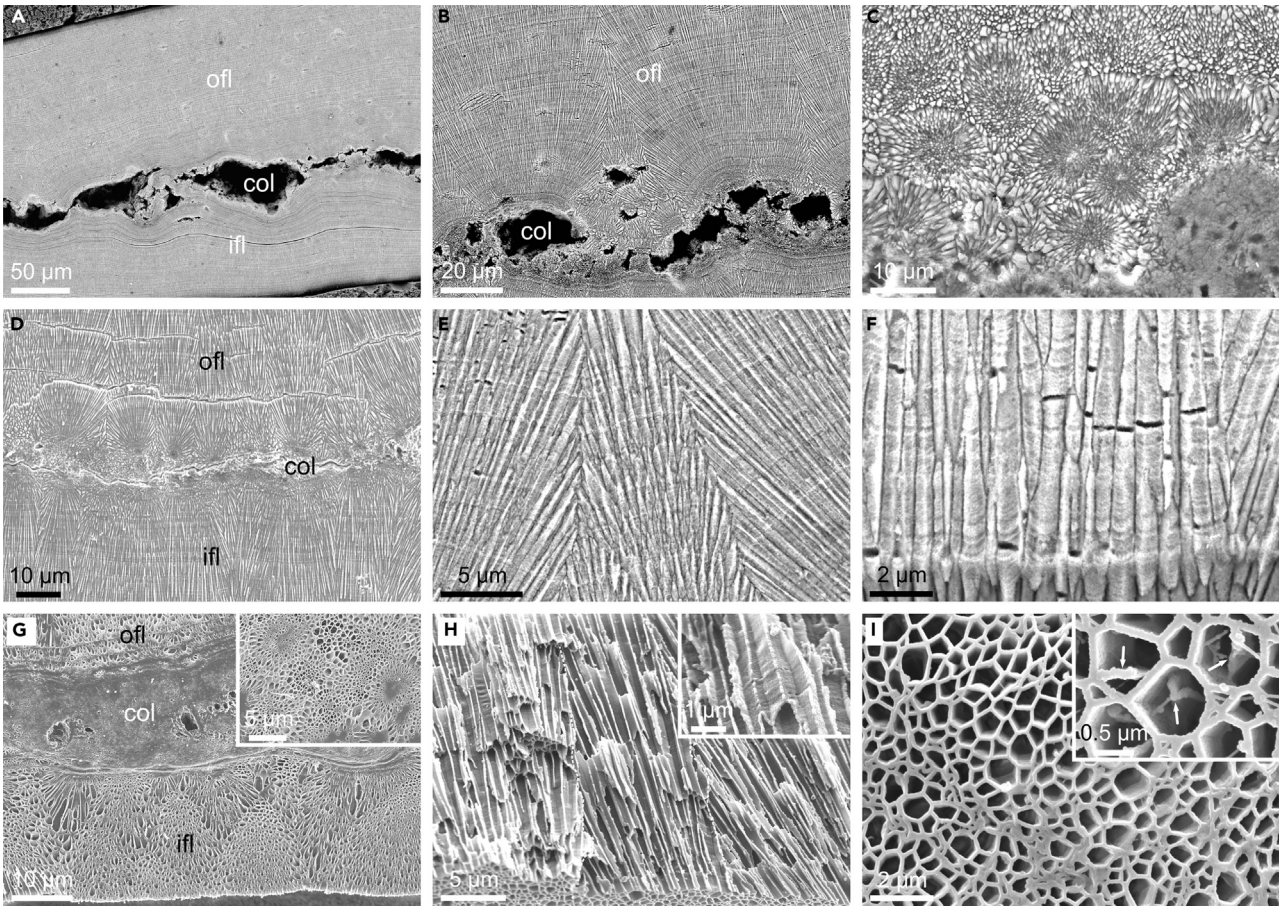

Figure 1. Microstructure of the shell of *Argonauta hians*

(A) Section of the shell showing the central organic layer and the two finely prismatic layers.

(B) Detail of the central part of the shell, where fibrous spherulitic arrangements initiate and grow toward both the outer and inner surfaces.

(C) Oblique cut through the initial spherulites.

(D) Competition between central spherulites. Note that the more obliquely oriented fibers become interrupted at the boundaries between spherulites and only those closer to the growth directions persist.

(E) Detail of the contacts between three spherulites showing interruption of oblique fibers at the boundaries.

(F) Detail of the fibers. Growth lines go uninterruptedly across them.

(G) Decalcified sample. The middle organic layer is marked by a non-differentiated organic mass. The spherulites on both sides of the central layer are replicated by the organic framework. The inset is a detail of the initial spherulites (compare with (C)).

(H) Detail of the organic sheaths of the fibers. The view is from an intermediate area between spherulites (the boundaries are indicated with broken lines). The inset is a detail showing the growth lines imprinted on the organic sheaths.

(I) Transverse section through the organic framework, showing its polygonal aspect. The inset is a detail. Note the incomplete membranes within some polygons (arrows). Col, central organic layer; ifl, inner fibrous layer; ofl, outer fibrous layer.

(TGA-DSC) revealed ~1.5% of structural water (weight loss up to 200°C) and 8.68% of organic matter (weight loss between 200% and 600%), that is, a total of 11.91% of amorphous material, notably higher than the amount calculated by XRD. This indicates that XRD may not be sensitive enough to quantify all amorphous components.

Fourier transform infrared (FTIR) spectra of the organic fraction (Figure S1) show strong protein peaks (Amide I and Amide II) and low-intensity absorption peaks in the polysaccharide region.

Shell structure and microstructure by electron and atomic force microscopy

Scanning electron microscopy (SEM) observations reveal that the shell consists of two finely prismatic or fibrous layers separated by a central organic layer (Figure 1A), as previously observed (Bøggild, 1930). At the boundaries of the central organic layer with both fibrous layers, there is a series of centers from which

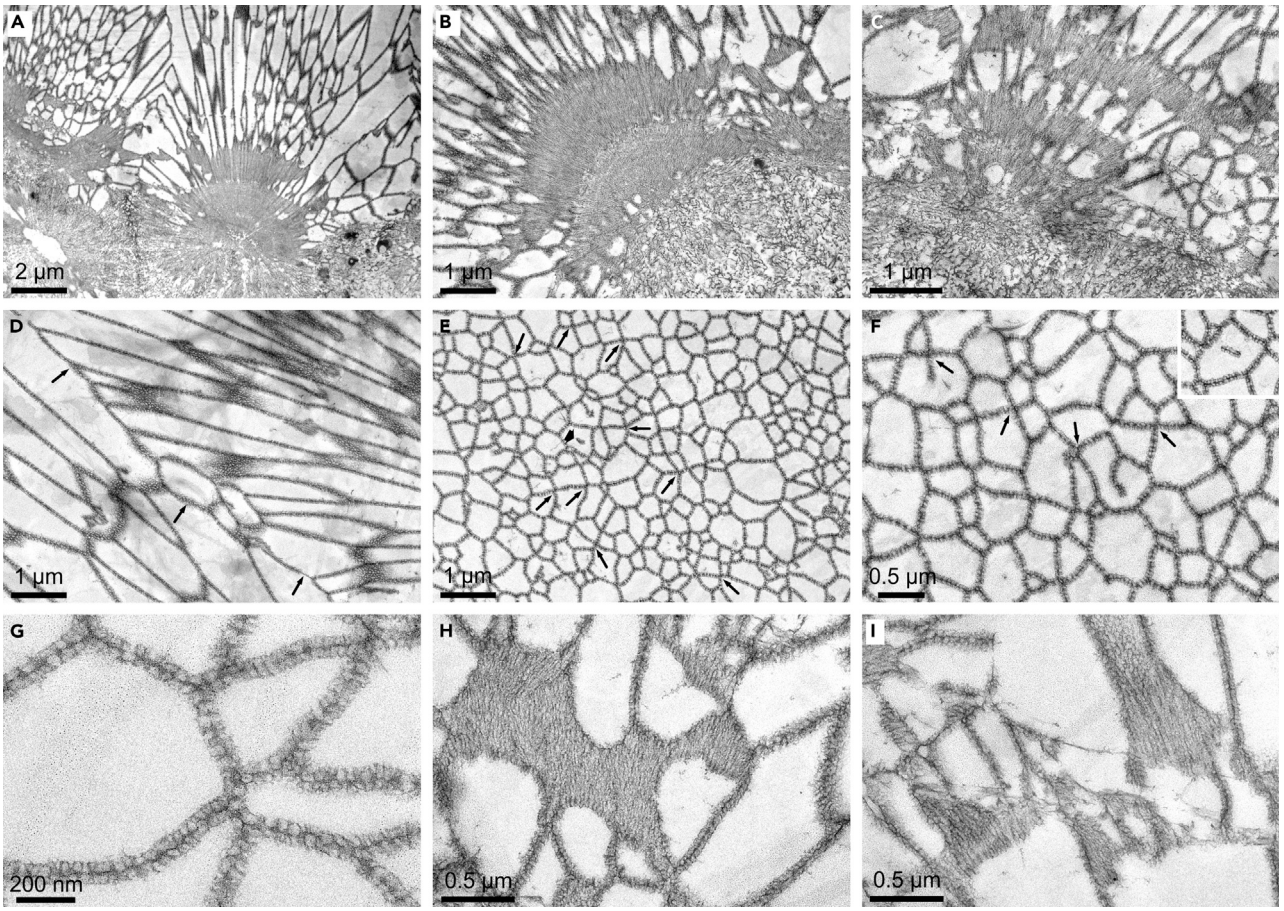

Figure 2. TEM views of the organic membranes of decalcified samples

(A) Longitudinal section across part of the central layer. The spherulites initiate from organic fibrous nuclei settled onto the less dense organic fabric of the central layer.

(B and C) Details of the nuclei. The initial organic nucleus in (B) has a fibrous radial aspect and is more compact than in (C).

(D) Detail of the contact between two spherulites, marked by organic membranes (arrows).

(E and F) Two views of a transverse section through the organic network, at different magnifications. Elements of the network have a clear polygonal outline, with sides that meet at triple points, or, more rarely, at quadruple points (arrows). Some incomplete membranes initiate from the sides, or in isolation from the central area (thick arrow in (E) and inset in (F)). Scale in (F) valid also for the inset.

(G) Detail of the membranes. They consist of a double layer of elements that appear rounded in this kind of section.

(H and I) Section slightly oblique to the membranes. The membranes have a fibrous aspect where the cut is subparallel to them (wide gray areas), demonstrating elements that elongate parallel to the growth direction of the membranes.

radiating arrangements of fibers (i.e., spherulites) initiate (Figures 1B–1D). Upon growth, they compete with each other, such that fibers become increasingly parallel (Figures 1D and 1E). Growth lines, marking the positions of the mineralizing tissue, extend uninterruptedly across the contiguous spherulites (Figures 1A, 1B, 1D, and 1E) and fibers (Figure 1F). Upon decalcification, the central layer reveals a high amount of organic substance and the material retains its whole spherulitic fibrous aspect (Figure 1G). In close view, the decalcified fibers consist of an organic network of membranes forming very elongated prismatic units with polygonal outlines (Figures 1H and 1I), as described (Kobayashi, 1971; Mitchell et al., 1994). Growth lines are imprinted on the surfaces of the membranes (Figure 1H, inset).

Transmission electron microscopy (TEM) examination provides additional details of the organic network. Sections perpendicular to the growth surfaces reveal that every spherulite has an initial dense organic-rich core, from which both the calcite fibers and the intervening membranes initiate (Figures 2A–2C). More to the interior of the central layer, the organic material looks looser. The boundaries between spherulites are marked by membranes (Figure 2D). Sections parallel to such surfaces reveal the reticulated pattern formed by the organic membranes (Figures 2E and 2F). It is formed by polygons with diameters between less than 100 nm to close to

2 μm. The number of sides ranges from three to eight, also depending on size. As previously indicated (Mitchell et al., 1994), the polygons resemble minimal surface structures whose sides meet at triple points, although quadruple points are not infrequent (Figure 2F). The organic pattern can be qualified as cellular, but we will avoid the term "cell" to refer to individual polygons in order to avoid confusion with the cells of the living tissue, referred to below. Frequently, membranes extend from one side toward the interior of the polygon and do not reach the opposite side (Figures 2E and 2F), something also observed under the SEM (Figure 1I, inset), and previously noticed (Mitchell et al., 1994). More rarely some short membranes appear isolated within single polygons (Figures 2E and 2F, inset). Membranes show consistent thicknesses between 70 and 90 nm, and are constituted by a double layer, separated by a distinct dark interphase a few nanometers thick (Figure 2G). In transverse section, each layer consists of aligned rounded elements, which, in longitudinal section, appear noticeably elongated (Figures 2B, 2C, 2H, and 2I). All the above implies that the organic walls are made by two adjoining palisades of fibers elongated in parallel to the growth direction and separated by a dark interphase a few nanometers thick.

TEM and atomic force microscopy (AFM) observations reveal that the calcite constituting the shell of *Argonauta* has an ultrastructure similar to that of most other calcium carbonate biominerals. TEM reveals the presence of wide amorphous rims (sometimes >10 nm) around the crystalline phase (Figures 3A and 3B), which can be recrystallized by beam radiation (Figure 3B). This argues for a minority ACC phase. AFM observations (tapping mode) (Figures 3C and 3D) reveal a distinct surface roughness, typical of biocrystals (Dauphin, 2008), with two phases with different contrast (phase mode): a lighter contrast phase forming the bulk of the structure and a dark minority phase in the form of threads (arrows in the amplitude and phase images of Figure 3D). Previous studies on other biocrystals interpreted the lighter phase as crystalline and the darker phase as ACC enriched in biomolecules (Macías-Sánchez et al., 2017; Seto et al., 2012). These studies also showed that the darker phase, when preserved adequately, is distributed as more or less continuous pellicles. The thread-like distribution we observe is most likely due to deficient preservation of the observed growth surfaces. Both AFM and TEM observations are consistent with the presence of a minor ACC component.

Evolution of the organo-mineral pattern during growth

The study by focused ion beam coupled with SEM (FIB-SEM)-aided slice and view allowed us to track the evolution of the organo-mineral network during growth. By merely observing the successive slices, one can appreciate that the network is in a permanent dynamic state, even for reduced thicknesses (scanned volume ZEISScan 1; see method details). Polygons can undergo three different processes: (1) enlarging, (2) shrinking (to disappearance), and (3) division into two or more daughter polygonal units by intercalation of new membranes. Particular examples can be seen in Figures 4A–4C and Video S1. When a membrane emerges from one of the sides, the latter, being initially flat, bends at the junction, such that the initial 90°-90°-180° junction tends to transform progressively into a triple junction at 120° (Figure 4C). The quadruple points observed are not permanent and split with growth into two separate triple points (Figure 4D). All these processes do not take place immediately, but after a certain, sometimes prolonged, growth (i.e., thickness) delay.

In order to determine if these processes obey particular rules, we tracked the changes in surface area of individual polygons within two selected groups (seven polygons initially each) during the growth of the fibrous layers in each of the scans TESScan 1 and ZEISScan 1 (see method details). The curves obtained show that small polygons (below a cross-sectional area threshold value) tend to shrink until disappearance, whereas large polygons tend to become larger (Figures 5 and S2). The threshold in the four groups selected is 0.2–0.3 μm^2 (Figures 5 and S2). Of interest, particularly large polygons tend to split due to the appearance of new membranes. In this way, the polygons split into two or, more rarely, three, sometimes in a repeated fashion (Figures 5B and S2A). In general, there is not a clear-cut threshold value for polygon splitting: the minimum values observed are in the order of 0.5 μm^2 (Figure S2B), although other polygons do not split until values $\geq$2 μm^2 (Figures 5A and S2).

The group of polygons shown in Figure S2B was selected close to a neighbor spherulite. Owing to the cut being oblique, the neighbor progressively invaded the group and gradually outcompeted the polygons. Some polygons became temporarily wholly incorporated within the neighbor before disappearance (Figure 4E, and two right crops at the top of Figure S2B). This explains why all ascending curves eventually acquired a negative slope, soon after they were reached by the polygons of the advancing front of the neighbor spherulite (blue arrows in Figure S2B).

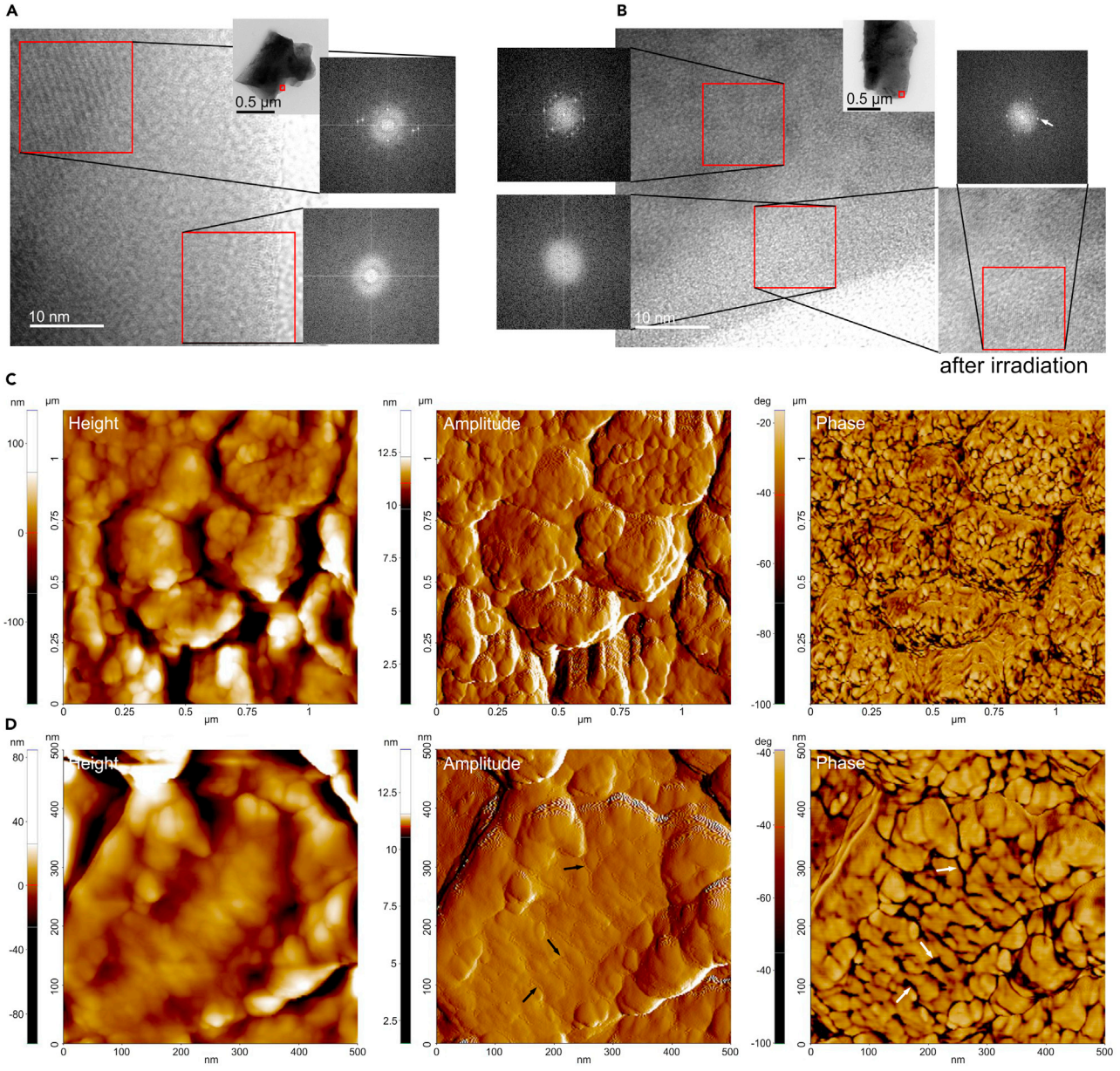

Figure 3. TEM and AFM analysis of the calcite of *Argonauta hians*

(A and B) TEM analysis of two particles obtained through grinding. The particles are the small upper insets and the areas analyzed are framed in red. In both cases, the particles are crystalline but the rims appear amorphous, as indicated by the high-resolution images and the fast Fourier transform (FFT) of the framed areas. In the particle in (B), the amorphous rim recrystallized (spots in the FFT) after 15 min of irradiation.

(C and D) AFM images of two different areas of the growth surface at different magnifications. The surfaces of the prisms display a characteristic roughness. The higher-magnification views in (D) show the existence of a low contrast (yellow-orange) background phase and a high-contrast (dark brown) phase, in the form of threads (arrows in phase image). The amplitude image shows that the threads are distributed between the nanoelevations of the surface (arrows in amplitude image).

For the whole ZEISScan1 area, containing hundreds of polygons, we have calculated the number of polygons (N), the mean surface area (Average Area) (Figure 6A), and the standard deviation (SD) (Figure 6B). Since SD is dependent on the mean size, we have also calculated the coefficient of variation (CV = SD/Average Area) (Figure 6B) as a measure of size distribution independent of the scale. A plot of these parameters versus the increase in thickness reveals that they all remain relatively constant during growth (Figure 6). If we replot these parameters after manually eliminating the newly formed membranes (i.e., by suppressing polygon splitting)

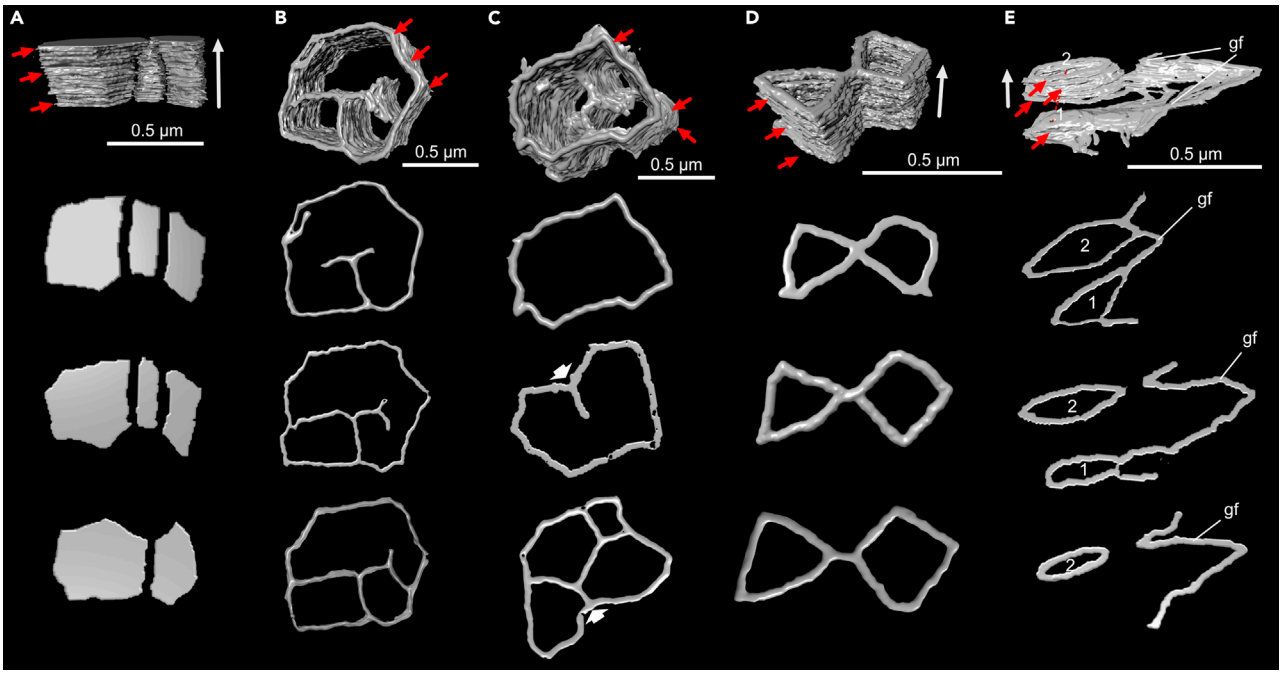

Figure 4. Examples of membrane dynamics revealed by slice and view

In each case, a 3D view is provided, together with three sections at different depths (bottom, top, and intermediate; red arrows)

(A) Example of polygon enlarging and shrinking. The two lateral polygons enlarge, while the central element (the smallest one) shrinks until disappearance.

(B and C) Examples of polygon splitting into three (B) or four (C). The thick arrows in (C) indicate transformation of the initially flat side into a triple joint due to the appearance of a new membrane. Growth direction is toward the background in the two cases.

(D) Transformation of a quadruple point into two triple points.

(E) Detachment of two polygons (1 and 2) from a spherulite and incorporation within the neighbor spherulite; gf is the growth front of the spherulite to which the two elements belong. Polygons 1 and 2 are the same as 7 and 4a in Figure S2B, respectively. Long white arrows in (A, D, and E) indicate the growth directions. Growth in (B and C) is toward the background. (A–D) were obtained from the scanned volume ZEISScan 1, whereas (E) was obtained from TESScan 1. The volume represented corresponds to the mineral infillings in (A) and to the organic sheaths in (B–E).

(eliminated membranes can be seen in Figure S3), there is a downward trend for N and a drastic upward trend for Average Area (curves labeled "nmr" in Figure 6), as expected. At the same time, SD increases and CV decreases slightly. This is easily explained because, in normal conditions, the splitting of large polygons compensates for the disappearance of small polygons, thus providing constant N and Average Area and keeping SD more or less constant. In the absence of splitting, large polygons continue to enlarge, thus accentuating the size differences (i.e., higher SD). The slight decrease of CV in the absence of splitting is caused by the increase of Average Area being somewhat faster than that of SD. Our procedure of eliminating the new divisions through the different slices does not provide a fully realistic solution, since splitting interrupts the trend of large polygons to continue growing. Splitting occasionally leads to particularly small polygons, which shrink with time (e.g., polygonal element 2b in Figure 5A and polygonal elements 2ba and 2bbb in Figure 5B). Foreseeably, in the absence of splitting, Average Area and SD should increase above our calculations. We cannot quite predict the behavior of CV since it depends on the change speed of the above two parameters. In summary, the splitting process of large polygons is responsible for keeping all the measured parameters constant throughout growth. All parameters, except for CV, correlated significantly with the thickness (Table S2).

A similar calculation was carried out on the much larger and deeper TESScan 2 volume (containing thousands of polygons and a depth of ~32 µm). The plots obtained (Figure S4) display accentuated fluctuations in the above parameters. This is due to the slicing going through growth bands with particularly small polygons, i.e., at a larger scale there are growth rhythms marked by changes in the relative productions of the organic/mineral phases.

Crystallography and distribution of the calcite phase

Electron backscatter diffraction (EBSD) orientation maps indicate that the calcite crystals of both the outer and inner fibrous layers are broadly oriented with their c-axes perpendicular to the outer and inner surfaces,

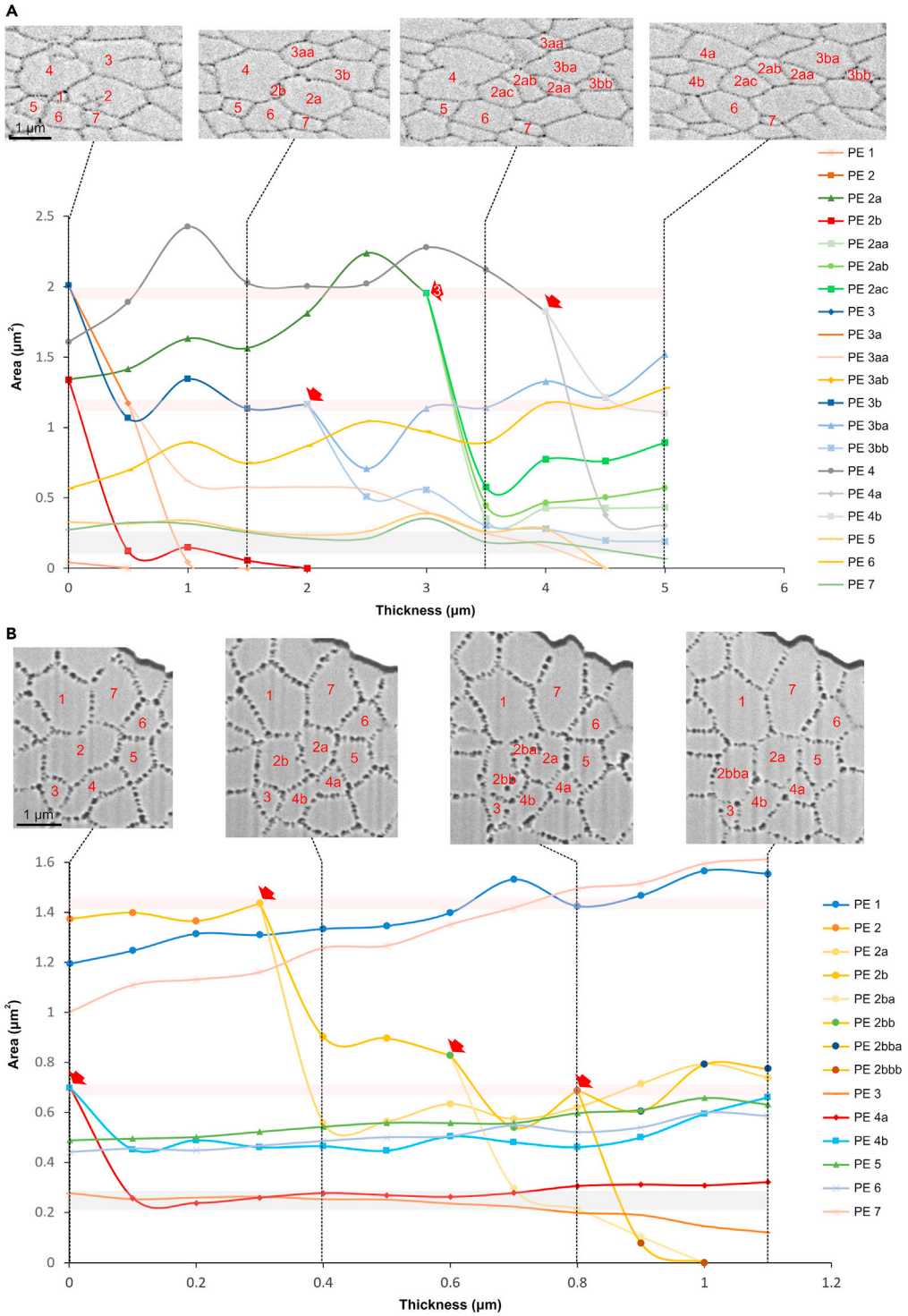

Figure 5. Surface area versus thickness plots of selected groups of polygonal elements (PEs)

(A and B) were selected from the TESScan 1 and ZEISScan 1 sliced volumes, respectively. The gray bands indicate the approximate size boundary above or below which PEs shrink or enlarge, respectively. The pink bands mark the lowermost and uppermost cases of splitting. Splitting events are indicated with thick arrows. Note splitting into three of PE 2a (arrow labeled with 3) in (A), and repeated splitting of PE 2 and its daughter PEs in (B). The upper crops display the distribution of PEs at different thicknesses.

See additional examples in Figure S2.

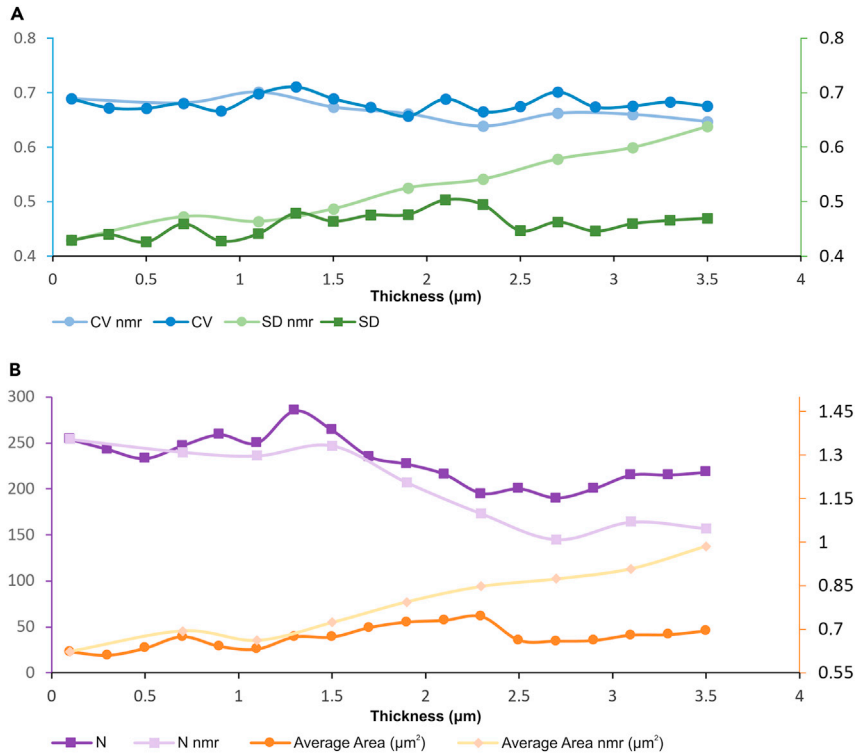

Figure 6. Plots of standard deviation (SD), coefficient of variation (CV) (A), number of polygons (N), and Average Area (B) versus Thickness for the ZEISScan 1 volume

The curves labeled "nmr" (new membranes removed), in lighter colors, are estimations of the same parameters by removing the membranes introduced during growth. Note differences in trends of parameters with and without the new membranes removed. The polygonal network and the removed membranes at three different thicknesses can be found in Figure S3.

See also Figure S4.

i.e., parallel to the growth direction (Figure 7A, left panel). The a-axes can take on any orientation around the c-axis. The resulting texture is a fiber or axial texture. Each spherulite initially consists of a few crystals whose c-axes are arranged in a fan-like orientation (Figure 7A, right panel). With growth, the crystals situated more to the sides of the spherulites disappear due to the impingement onto the neighbor spherulites. In this way, both the number of crystals composing a given spherulite and the spread of their c-axes become reduced with growth. All in all, there is a greater spread of orientations close to the central organic layer, which soon becomes reduced with the impingement onto adjacent spherulites.

The cropping of particular domains, each identifiable by a reduced three-dimensional crystallographic orientation spread (see method details), reveals their complex outlines. In sections transverse to the growth direction spherulites take shapes similar to fractal coastlines, with differently sized and shaped capes and gulfs (Figures 7B and S5A). Some even engulfed bits of adjacent domains (white arrows in Figure 7B, and red arrows in Figure S5A). The latter two features can be explained by the interactions between prismatic units of contiguous spherulites, as explained above (Figures 4F and S2B). The same pattern is observed in sections parallel to the growth direction (Figure S5B). In high-resolution Kikuchi diffraction band maps, the outlines of the polygons formed by the organic membranes appear as dark lines, as they do not give Kikuchi diffraction intensities (Figure 7C, left panel). In Figure 7C, central panel, the outlines of four domains, which have been isolated in the orientation map of Figure 7C, right panel, have been superposed onto the Kikuchi band contrast map. The comparison between the three panels shows that domains are always bounded by the organic walls, i.e., they are confined within the organic walls, and contain integral polygons. This indicates that the mineral phase behavior is subordinated to that of the organic phase. The observed relationship is worth commenting on. As observed under the TEM, the organic membranes initiate from the organic centers of the spherulites present on both sides of the central organic layer (Figures 2A–2C).

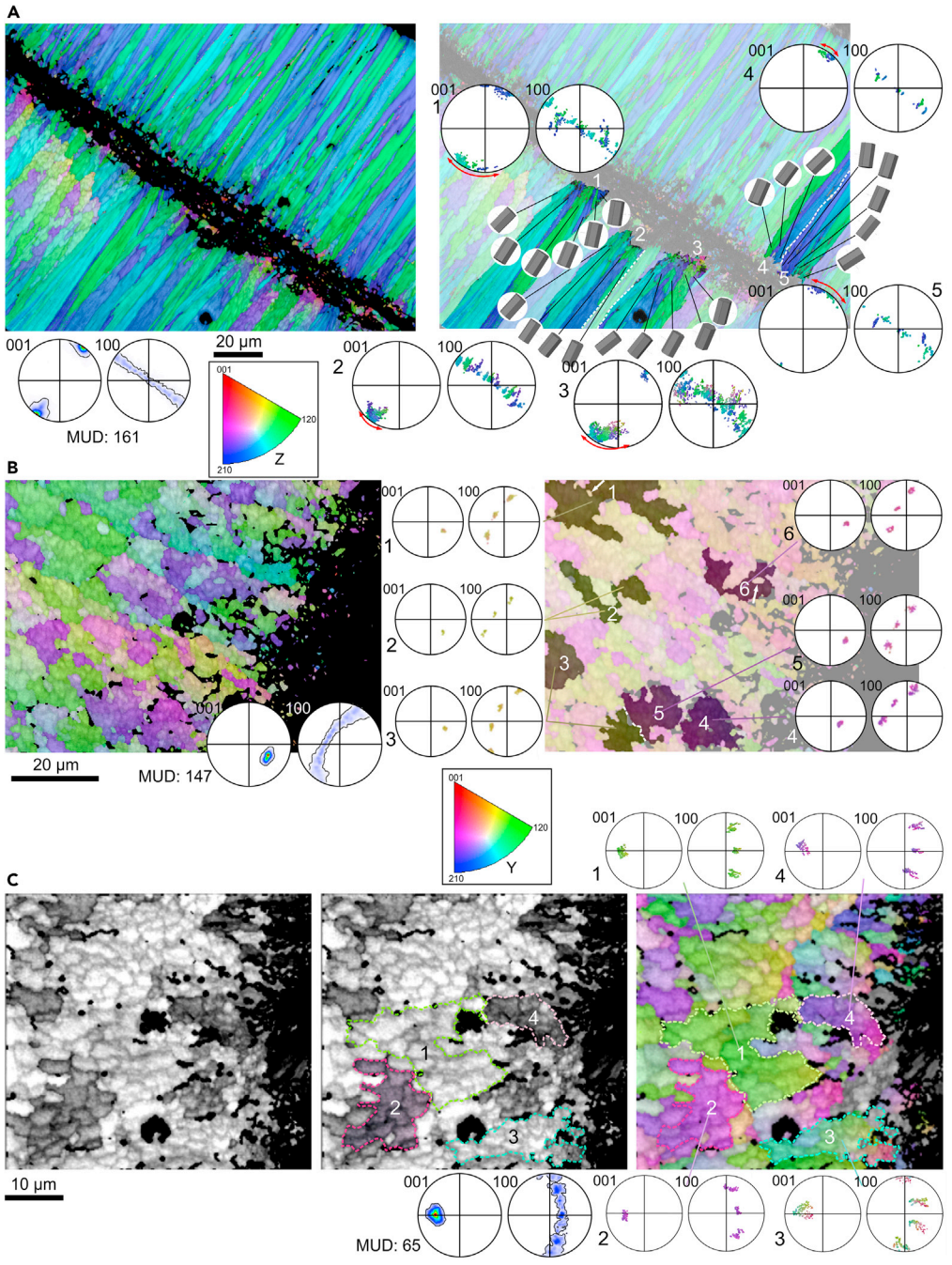

Figure 7. Crystallography of the calcite phase and its spatial relation with the organic framework

The crystallographic indices ((001) for calcite c-axes and (100) for calcite a*-axes) are Miller indices (i.e., plane normals) referring to the "hexagonal" unit cell of calcite. The color images are representations of crystallographic orientations; the latter are shown color coded, relative to a defined color code (color triangles in (A and B))

(A) EBSD map of a section perpendicular to the shell surface across the middle organic layer (left). The pole figures indicate that the c-axes are parallel to the axes of elongation of the fibers. In the right panel, five spherulites have been cropped out and analyzed individually. Analysis of the lattice orientation within domains indicates that the c-axes within each spherulite have a radial orientation. The spreads of the c-axis orientation are indicated in the (001) pole figures with red arrows.

(B) EBSD map of a section transversal to the fibers. Some domains (each characterized by a particular crystallographic orientation) have been isolated. They have very complex, fractal-like outlines. Some of them have engulfed portions of other domains (white arrows).

Figure 7. *Continued*
(C) High-resolution EBSD map of a section transversal to the morphological axis of the fibers. The left panel is the EBSD band contrast measurement map, and the central panel is the same map with the boundaries of four domains indicated with broken lines. The organic membranes appear as dark lines as they do not give a band contrast, Kikuchi diffraction signal in both the left and central panels. The four domains indicated in the central panel are analyzed individually in the right panel, which is the EBSD orientation map. The comparison between the three maps shows that the domains are bounded by organic membranes. In all cases, the crystallographic textures derived from the orientation maps are axial textures. MUD values (see method details section) indicate a good co-orientation in the maps shown in (A and B), and medium in that in (C), Note that within each map there is little difference in the c-axis or the (001) orientations; the main difference is in the a*-axis or the (100) orientations. Key color in (B), valid also for (C).
See also Figure S5.

The crystals presumably nucleate onto the organic center and must already be bounded by the formed organic membranes at this early stage. We do not know if there is a one to one crystal domain/organic prism relationship. During further growth, some polygons and their domains will be eliminated, while the process of splitting will allow a given domain to extend over two or more polygons. Repeated splitting could explain why crystal domains extend over many polygons.

Crystal competition has been reported in biomineral aggregates (Crippa et al., 2020; Goetz et al., 2009; Rodríguez-Navarro and García-Ruiz, 2000) and was invoked also in the shell of *Argonauta hians* based on an increase of the EBSD-determined multiple of uniform distribution (MUD) values (which are a measure of crystal co-orientation; see method details) with growth (e.g., Stevens et al., 2017). Nevertheless, direct crystal contact (i.e., competition) is not expected since the calcite crystals are confined within the organic membranes. In fact, the outlines of crystal domains are not of the crystalline type (Figures 7 and S5). An increase in the MUD values can also be expected from the competition observed at the boundaries between spherulites, where the more oblique fibers containing the more inclined crystals (Figure 7A, right panel) are progressively eliminated with growth (Figures 1B, 1D, and 1E), i.e., competition between polygons may lead to an apparent competition between crystalline domains.

DISCUSSION

The shell mineralogy of the female *Argonauta* is fully calcitic, with a high amount of Mg (<10% molar substitution). This is 2-fold the previously reported value (Wolfe et al., 2012, 2013), and several-fold above any other molluscan calcite, always low-Mg calcite (e.g., Freitas et al., 2005). The amount of organic matter calculated by TGA-DSC (<8.5%) is notably higher than the amount calculated by XRD, and is in striking contrast with the ~1.8% of organic matter calculated by Oudot et al. (2020) after extraction by dissolution and ultrafiltration. The latter might be a low estimate since part of the biomolecules may have been lost during extraction. FTIR data indicate a significant predominance of proteins and is in agreement with previous results on the acid-insoluble matrix fraction of *Argonauta hians* (Oudot et al., 2020).

The shell of the female *Argonauta* is not secreted by the mantle of the animal, as in all mollusks, but by a completely separate tissue: the webs of the two dorsal arms. Accordingly, it is not homologous to the shell of mollusks, but an innovation of the Argonautidae, dating from the Late Oligocene (Noda et al., 1986). Hence, it is not surprising that, compared with the shells of mollusks, it is unusual in (1) its fully calcitic nature (calcitic bivalves, such as oysters, retain an aragonitic myostracum and intraligamentary fibers), (2) the high-Mg chemistry of the calcite, and (3) the bidirectional growth (toward the interior and the exterior of the shell) of the fibrous layers.

The organic network, when observed in transversal section, constitutes a polygonal cellular pattern with a minimal energy configuration, characterized by triple junctions at ~120° (Plateau's law). We have also found that the polygonal network follows the von Neumann-Mullins topological law (Mullins, 1956; Von Neumann, 1952) during growth, since the individual polygons above a certain size (cross-sectional area) threshold (estimated here at 0.2–0.3 μm^2) continue to enlarge, whereas those below that threshold shrink until disappearance. Similar behavior was demonstrated in the calcitic prismatic shell of the bivalve *Pinna nobilis* (Bayerlein et al., 2014), which was interpreted as a case of normal grain growth. Alternatively, Checa et al. (2016a) attributed such behavior in this and related species to the thick organic membranes surrounding the mineral units. They proposed that the system evolves as a biliquid foam or emulsion created between the fluid precursors of both the mineral, the so-called PILP (Olszta et al., 2003; Schenk et al., 2012), and the organic phases (gel-like precursor). In the prismatic layers of bivalves, given the relative

dimensions of the extrapallial space (EPS) (~100 nm thick), the mineral prismatic units (tens of micrometers in diameter), and the organic membranes (1–5 μm in thickness), it seemed unlikely that the mineral and organic components, if poured together to the EPS, could diffuse to their corresponding positions in the mineral units and organic membranes, respectively. Also, given the diameters (<10 μm) of the outer mantle cells (OMCs), below the mineral units' diameters and above the organic membranes' thicknesses, several OMCs must cooperate in the secretion of a single prismatic unit. Some OMCs would fall entirely below a mineral unit and would only secrete mineral components. Conversely, others would be in contact with the intervening organic membrane and would secrete either mineral or organic precursors in different areas of their surface, depending on which material they are in contact with. Accordingly, OMCs must recognize the substrate previously secreted, through contact recognition, and use it as a template for further secretion. This kind of secretion requires strict orchestration of the adjoining OMCs. Similar cellular recognition processes were invoked for the formation of the calcitic fibrous microstructure of brachiopods (Simonet Roda et al., 2019), the aragonitic helical fibrous microstructure of some planktonic gastropods (Checa et al., 2016b), and the vesicular microstructure of some oysters (Checa et al., 2020). Substrate recognition by cells is widespread in biological processes, like cell aggregation, growth, or immune response (Culp, 1978; Obrink and Ocklind, 1983; Saier and Jacobson, 1984). Recognition is carried out by cell surface receptors, able to identify ligands (both receptors and ligands are particular biomolecules) present in the substrate. This mechanism is also developed by mollusks (Gerdol et al., 2018). It is exploited in biomimetic science to develop bioadhesive and biocompatible materials by coating their surfaces with cell-recognizable natural proteins (Rahmany and Van Dyke, 2013).

We have demonstrated that in the shell of *Argonauta* the organic framework dominates the pattern and evolves following the laws of emulsions, foams, and metallic grain aggregates. As explained above for the prismatic layers of bivalves (Checa et al., 2016a), of these three possibilities only a system fluid-fluid is biophysically possible, that is an emulsion between the mineral and organic fluid precursors created at the interface between the mineralized shell and the living tissue (Figure 8). Our ultrastructural AFM and TEM data on the calcite of *Argonauta* indicate that its nanostructure is identical to that of other biominerals, including the presence of residual ACC. Accordingly, we can safely assume that the high-Mg calcite crystallizes from an ACC precursor, as in invertebrate biocrystals (Addadi et al., 2003), most likely in the form of a PILP, generated by acidic biopolymers (Olszta et al., 2003). It has recently been found that the PILP for calcium carbonate consists of ACC nanoclusters, with liquid-like behavior (Xu et al., 2018), i.e., it is a colloidal phase. The organic phase (the membrane network) would constitute the continuous phase of the emulsion. The membranes are constituted by highly organized self-assembled double layers of fibrous proteins. Proteins play important roles in emulsions, particularly as stabilizers (e.g., in Pickering-type emulsions) (Cabra et al., 2008; Hoffman and Röge, 2014), to which they impart gel-like properties (emulgels) (Glusac et al., 2018; Sun and Holley, 2011).

In *Argonauta*, virtually nothing is known about the characteristics of the biomineralization system created between the forming shell and the webs of the dorsal arms. Nevertheless, given the smoothness and continuity of the growth lines (Figures 1A, 1B, and 1D–1F), we may hypothesize that the dorsal webs must be very close to the shell growth surface during secretion (Figure 8), in a way similar to the mantle of the rest of shell-forming mollusks. Compared with the prismatic layers of bivalves, the surface areas of polygons in *Argonauta* (rarely above 1 μm^2) are much smaller than those of the biomineralizing living cells of the dorsal webs (DWCs). Although there may be some doubt on the involvement of contact recognition processes in the formation of the argonaut shell, there is a process unique to it that makes such processes ineluctable: polygon splitting. This feature cannot be driven physically because it acts against the reduction of the free energy of the system (the number of interfaces), according to the von Neumann-Mullins law. Polygon splitting undisputably demands that the living DWCs are able to locate the polygons exceeding a certain cross-sectional area and extend new membranes across them (Figure 8). Note that the membranes in *Argonauta* are much thinner (>100 nm) than those of the prismatic layers of bivalves (1 to several micrometers) (Checa et al., 2016a), which speaks about the sensitive abilities of the DWCs, i.e., recognition and secretion takes place well at the submicron level. Given the continuity of the organic framework, there must be a coordinated and refined recognition-secretion activity of the mineralizing DWCs. Frequently, the production of new membranes and the detection of large polygons will be shared by two or more neighbor DWCs, since those objects do not necessarily fall within the ambitus of single DWCs. Accordingly, the implicated DWCs must act in coordination to carry out their secretory/sensitive activity. A recent proteomic study (Oudot et al., 2020) found that the organic matrix of *Argonauta hians* contained several hits with proteins that bind to signaling molecules. These might easily derive from the DWC activity we invoke here.

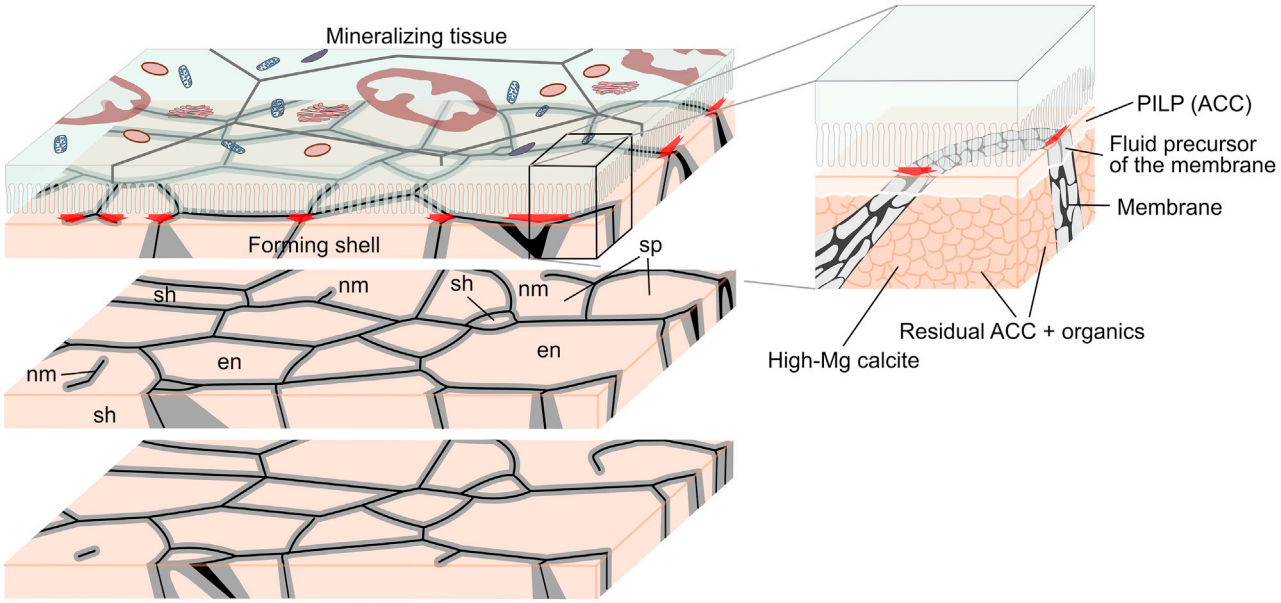

Figure 8. Evolution of the organo-mineral pattern during growth of the fibrous layer of *Argonauta hians* and model for its fabrication

Figure360▷ For a Figure360 author presentation of this figure, see https://doi.org/10.1016/j.isci.2021.103288.

Left, sketch depicting the different processes of polygon dynamics across three shell slices. en, polygon enlargement; nm, development of new membranes; sh, polygon shrinking; sp, polygon splitting. The right sketch is a detail of the processes taking place at the interface between the mineralized shell and the mineralizing tissue. The organomineral pattern grows from an emulsion between the PILP (essentially ACC + organics) and the fluid precursor of the membranes. After the PILP is transformed into the high-Mg calcite of the shell, residual ACC enriched in (and stabilized by) organics remains in the form of pellicles. At every growth increment, the mineralizing tissue of the dorsal web adheres to the shell growth surface and "senses" (red arrows) the position and distribution of the organic network. In this way, the pattern is continued according to (1) the physics imposed by the emulsion and (2) the introduction of new membranes where particularly large polygons have been located by the cells of the dorsal web.

We found that the threshold for enlargement/shrinking of the polygons is narrow (calculated here between 0.2 and 0.3 μm^2), whereas that for polygon partition is very wide (0.7–2.2 μm^2). The difference lies in that the former is determined by a physical process (emulsion coarsening), whereas the second has a biological basis (location of particularly large polygons by the DWCs and subsequent secretion), with a much wider control range.

Polygon splitting clearly aims at maintaining mean cross-sectional surface area (Average Area) and area distribution (SD and CV; the latter being called polydispersity in colloidal systems) constant throughout growth. There might be a functional reason behind it. The organic membranes of the prismatic layers of bivalves make the material highly elastic. These materials constitute the margins of bivalves of the order Ostreida and flex upon valve closure, thus providing a tight marginal seal (Harper and Checa, 2020). Power (1856) reported that the shell of *Argonauta argo* is also highly flexible. Accordingly, maintaining the density of organic interfaces constant (by polygon splitting) would permit to retain the flexibility upon shell thickening.

Limitations of the study

Technically, the study was limited by the quality of the FIB-prepared surfaces. Despite the use of a rocking stage to minimize the curtain effect (see method details), some of the images had to be manipulated by hand, owing to the incompleteness of the organic boundaries. From the conceptual viewpoint, a main shortcoming is the virtual absence of information about the biomineralization system in *Argonauta*, particularly with regard to the structure of the biomineralizing tissue of the dorsal webs and its position with respect to the shell surfaces. We had neither access to living specimens nor the means to keep them in aquarium. Even if this had been the case, we would have been faced with the almost impossibility to keep the webs in position during specimen preparation for histological study. The inference we make of an extremely thin extrapallial space is based on the comparison with some known cases of the molluscan mantle, and on the evenness of growth surfaces. There is no expectation that this gap in knowledge can be filled in the short to medium term.

STAR★METHODS

Detailed methods are provided in the online version of this paper and include the following:

- KEY RESOURCES TABLE
- RESOURCE AVAILABILITY
  - Lead contact
  - Materials availability
  - Data and code availability
- EXPERIMENTAL MODEL AND SUBJECT DETAILS
  - Shells
- METHOD DETAILS
  - X-Ray diffraction (XRD)
  - Thermogravimetry (TGA) and differential scanning calorimetry (DSC)
  - Fourier-transform infrared spectroscopy (FTIR)
  - Atomic force microscopy (AFM)
  - Scanning electron microscopy (SEM)
  - Electron backscatter diffraction (EBSD)
  - 3D reconstruction by focused ion beam coupled to SEM (FIB-SEM)
  - Transmission electron microscopy (TEM)
  - Illustration
  - Video production
- QUANTIFICATION AND STATISTICAL ANALYSIS

SUPPLEMENTAL INFORMATION

Supplemental information can be found online at https://doi.org/10.1016/j.isci.2021.103288.

ACKNOWLEDGMENTS

We acknowledge TESCAN and Carl Zeiss Microscopy GmbH for the acquisition and early processing of the images by FIB-SEM. This research was funded by projects CGL2017-85118-P (A.G.C., C.G.), PID2020-116660GB-I00 (A.G.C., C.G., A.B.R.-N.) (Spanish Ministerio de Ciencia e Innovación), and B-RNM-265-UGR18 (A.G.C., C.G., A.B.R.-N.) (Junta de Andalucía), the Unidad Científica de Excelencia UCE-PP2016-05 (A.G.C., C.G., A.B.R.-N.) (University of Granada), and the Research Group RNM363 (A.G.C., C.G.) (Junta de Andalucía).

AUTHOR CONTRIBUTIONS

Conceptualization: A.G.C.; methodology: A.G.C., F.L., A.B.R.-N., and E.G.; investigation and formal analysis: all authors; visualization: A.G.C., F.L.; writing – original draft: A.G.C.; writing – review & editing: F.L., C.G., E.G., A.B.R.-N., W.W.S.

DECLARATION OF INTERESTS

The authors declare no competing interests.

Received: August 15, 2021
Revised: September 29, 2021
Accepted: October 13, 2021
Published: November 19, 2021

REFERENCES

Adams, H., and Adams, A. (1858). The Genera of the Recent Mollusca; Arranged According to Their Organization (John Van Voorst).

Addadi, L., Raz, S., and Weiner, S. (2003). Taking advantage of disorder: amorphous calcium carbonate and its roles in biomineralization. Adv. Mater. *15*, 959–970. https://doi.org/10.1002/adma.200300381.

Bandel, K., and Dullo, W.C. (1984). Zur Schalenstruktur fossiler und rezenter *Argonauta*-Gehäuse (Octopoda, Cephalopoda). Natur. Mensch. *1984*, 33–38.

Bayerlein, B., Zaslansky, P., Dauphin, Y., Rack, A., Fratzl, P., and Zlotnikov, I. (2014). Self-similar mesostructure evolution of the growing mollusc shell reminiscent of thermodynamically driven grain growth. Nat. Mater. *13*, 1102–1107. https://doi.org/10.1038/nmat4110.

Belcher, A.M., Wu, X.H., Christensen, R.J., Hansma, P.K., Stucky, G.D., and Morse, D.E. (1996). Control of crystal phase switching and orientation by soluble mollusc-shell proteins. Nature *381*, 56–58. https://doi.org/10.1038/381056a0.

Bourget, E. (1987). Barnacle shells: composition, structure, and growth. In Crustacean Issues: Barnacle Biology, *Vol. 5*, A.J. Southward and A.A. Balkema, eds., pp. 267–285.

Bøggild, O.B. (1930). The shell structure of the mollusks. K. Dan. Vidensk. Selsk. Skr. Naturvidensk. Math. Afd. *9*, 231–326.

Cabra, V., Arreguín, R., and Farres, A. (2008). Emulsifying properties of proteins. Bol. Soc. Quím. Méx. *2*, 80–98.

Carter, J.G., Harries, P.J., Malchus, N., Sartori, A.F., Anderson, L.C., Bieler, R., Bogan, A., Coan, E.E., Cope, J., Cragg, S., et al. (2012). Illustrated Glossary of the Bivalvia. In Treatise Online, Part N, Revised, Chapter 31, *Vol. 1*Treatise Online, Part N, Revised, Chapter 31 (Kansas University Paleontological Institute), pp. 1–209.

Cartwright, J.H.E., and Checa, A.G. (2007). The dynamics of nacre self-assembly. J. R. Soc. Interf. *4*, 491–504. https://doi.org/10.1098/rsif.2006.0188.

Checa, A. (2018). Physical and biological determinants of the fabrication of molluscan shell microstructures. Front. Mar. Sci. *5*, 353. https://doi.org/10.3389/fmars.2018.00353.

Checa, A.G., Macías-Sánchez, E., Harper, E.M., and Cartwright, J.H.E. (2016a). Organic membranes determine the pattern of the columnar prismatic layer of mollusc shells. Proc. Biol. Sci. *283*, 20160032. https://doi.org/10.1098/rspb.2016.0032.

Checa, A.G., Macías-Sánchez, E., and Ramírez-Rico, J. (2016b). Biological strategy for the fabrication of highly ordered aragonite helices: the microstructure of the cavolinioidean gastropods. Sci. Rep. *6*, 25989. https://doi.org/10.1038/srep25989.

Checa, A.G., Linares, F., Maldonado-Valderrama, J., and Harper, E.M. (2020). Foamy oysters: vesicular microstructure production in the Gryphaeidae via emulsification. J. R. Soc. Interf. *17*, 20200505. https://doi.org/10.1098/rsif.2020.0505.

Crippa, G., Griesshaber, E., Checa, A.G., Harper, E.M., Simonet Roda, M., and Schmahl, W.W. (2020). Orientation patterns of aragonitic crossed-lamellar, fibrous prismatic and myostracal microstructures of modern *Glycymeris* shells. J. Struct. Biol. *212*, 107653. https://doi.org/10.1016/j.jsb.2020.107653.

Culp, L.A. (1978). Biochemical determinants of cell adhesion. Curr. Top. Membr. Transp. *11*, 327–396. https://doi.org/10.1016/S0070-2161(08)60752-2.

Dauphin, Y. (2008). The nanostructural unity of mollusk shells. Mineral. Mag. *72*, 243–246. https://doi.org/10.1180/minma g.2008.072.1.243.

Dos Santos, H., Neumann, R., and Ávila, C.A. (2017). Mineral quantification with simultaneous refinement of Ca-Mg carbonates non-stoichiometry by X-ray diffraction, Rietveld method. Minerals *7*, 164. https://doi.org/10.3390/min7090164.

Falini, G., Albeck, S., Weiner, S., and Addadi, L. (1996). Control of aragonite or calcite polymorphism by mollusk shell macromolecules. Science *271*, 67–69. https://doi.org/10.1126/science.271.5245.67.

Finn, J.K. (2013). Taxonomy and biology of the Argonauts (Cephalopoda: Argonautidae) with particular reference to Australian material. Molluscan Res. *33*, 143–222. https://doi.org/10.1080/13235818.2013.824854.

Freitas, P., Clarke, L.J., Kennedy, H., Richardson, C., and Abrantes, F. (2005). Mg/Ca, Sr/Ca, and stable-isotope ($\delta^{18}O$ and $\delta^{13}C$) ratio profiles from the fan mussel *Pinna nobilis*: Seasonal records and temperature relationships. Geochem. Geophys. Geosyst. *6*, Q04D14. https://doi.org/10.1029/2004GC000872.

Gerdol, M., Gómez-Chiarri, M., Castillo, M.G., Figueras, A., Fiorito, G., Moreira, R., Novoa, B., Pallavicini, A., Ponte, G., Roumbedakis, K., et al. (2018). Immunity in molluscs: recognition and effector mechanisms, with a focus on Bivalvia. In Advances in Comparative Immunology, E.L. Cooper, ed. (Springer), pp. 225–341.

Glusac, J., Davidesko-Vardi, I., Isaschar-Ovdat, S., Kukavica, B., and Fishman, A. (2018). Gel-like emulsions stabilized by tyrosinase-crosslinked potato and zein proteins. Food Hydrocoll. *82*, 53–63. https://doi.org/10.1016/j.foodhyd.2018.03.046.

Goetz, A.J., Griesshaber, E., Neuser, R.D., Lüter, C., Hühner, M., Harper, E., and Schmahl, W.W. (2009). Calcite morphology, texture and hardness in the distinct layers of rhynchonelliform brachiopod shells. Eur. J. Mineral. *21*, 303–315. https://doi.org/10.1127/0935-1221/2009/0021-1922.

Griesshaber, E., Yin, X., Ziegler, A., Kelm, K., Checa, A., Eisenhauer, A., and Schmahl, W.W. (2018). Patterns of mineral organization in carbonate biological hard materials. In Highlights in Applied Mineralogy, S. Heuss-Aßbichler, S.G. Amthauer, and M. John, eds. (De Gruyter), pp. 245–272. https://doi.org/10.1515/9783110497342-012.

Harper, E.M., and Checa, A.G. (2020). Tightly shut: flexible valve margins and microstructural asymmetry in pterioid bivalves. Mar. Biol. *167*, 78. https://doi.org/10.1007/s00227-020-03693-y.

Heywood, B.R. (1994). Biomineralization: new directions in crystal science. Microsc. Res. Tech. *27*, 376–388. https://doi.org/10.1002/jemt.1070270504.

Hoffman, H., and Röge, M. (2014). Emulsions with unique properties from proteins as emulsifiers. Adv. Colloid Interf. Sci. *205*, 94–104. https://doi.org/10.1016/j.cis.2013.08.007.

Kobayashi, I. (1971). Internal microstructure of the shell of *Argonauta argo*. Venus *30*, 103–112.

Lowenstam, H.A., and Weiner, S. (1989). On Biomineralization (Oxford University Press).

Macías-Sánchez, E., Willinger, M.-G., Pina, C.M., and Checa, A.G. (2017). Transformation of ACC into aragonite and the origin of the nanogranular structure of nacre. Sci. Rep. *7*, 12728. https://doi.org/10.1038/s4159 8-017-12673-0.

Marin, F. (2020). Mollusc shellomes: past, present and future. J. Struct. Biol. *212*, 107583. https://doi.org/10.1016/j.jsb.2020.107583.

Miner, R.W. (1935). Marauders of the sea. Natl. Geogr. Mag. *68*, 185–207.

Mitchell, P.R., Phakey, P.P., and Rachinger, W.A. (1994). Ultrastructural observations of the argonaut shell. Scanning Microsc. *8*, 35–46.

Mullins, W.W. (1956). Two-dimensional motion of idealized grain boundaries. J. Appl. Phys. *27*, 900–904.

Noda, H., Ogasawara, K., and Nomura, R. (1986). Systematic and paleobiogeographic studies on the Japanese Miocene argonautid "*Nautilus*" *izumoensis*. Sci. Rep. Inst. Geosci. Univ. Tsukuba B, Geol. Sci. *7*, 15–42.

Obrink, B., and Ocklind, C. (1983). Cell–cell recognition: relation to cell adhesion with special reference to adhesion of hepatocytes. Blood Cell *9*, 209–219.

Olszta, M.J., Odom, D.J., Douglas, E.P., and Gower, L.B. (2003). A new paradigm for biomineral formation: mineralization via an amorphous liquid-phase precursor. Connect. Tissue Res. *44*, 326–334. https://doi.org/10.1080/713713604.

Oudot, M., Ben Shir, I., Schmidt, A., Plasseraud, L., Broussard, C., Neige, P., and Marin, F. (2020). A Nature's curiosity: the argonaut "shell" and its organic content. Crystals *10*, 839. https://doi.org/10.3390/cryst10090839.

Pokroy, B., Fitch, A.N., Marin, F., Kapon, M., Adir, N., and Zolotoyabko, E. (2006). Anisotropic lattice distortions in biogenic calcite induced by intra-crystalline organic molecules. J. Struct. Biol. *155*, 96–103. https://doi.org/10.1016/j.jsb.2006.03.008.

Power, J. (1856). Observations Physiques sur le Poulpe de l'*Argonauta argo*, commencées en 1832 et terminées en 1843 (Charles de Mourgues Frères).

Rahmany, M.B., and Van Dyke, M. (2013). Biomimetic approaches to modulate cellular adhesion in biomaterials: a review. Acta Biomater. *9*, 5431–5437. https://doi.org/10.1016/j.actbio.2012.11.019.

Rodríguez-Navarro, A., and García-Ruiz, J.M. (2000). Model of textural development of layered aggregates. Eur. J. Mineral. *12*, 609–614. https://doi.org/10.1127/ejm/12/3/0609.

Saier, M.H., and Jacobson, G.R. (1984). Cellular recognition: mechanisms and consequences of homotypic and heterotypic adhesions. In The Molecular Basis of Sex and Differentiation, M.H. Saier and G.R. Jacobson, eds. (Springer), pp. 135–157.

Schenk, A.S., Zope, H., Kim, Y.-Y., Kros, A., Sommerdijk, N.A.J.M., and Meldrum, F.C. (2012). Polymer-induced liquid precursor (PILP) phases of calcium carbonate formed in the presence of synthetic acidic polypeptides—relevance to biomineralization. Faraday Discuss. *159*, 327–344. https://doi.org/10.1039/C2FD2 0063E.

Schneider, C.A., Rasband, W.S., and Eliceiri, K.W. (2012). NIH Image to ImageJ: 25 years of image analysis. Nat. Methods *9*, 671–675. https://doi.org/10.1038/nmeth.2089.

Seto, J., Ma, Y., Davis, S.A., Meldrum, F., Gourrier, A., Kim, Y.-Y., Schilde, U., Sztucki, M., Burghammer, M., Maltsev, S., et al. (2012). Structure-property relationships of a biological mesocrystal in the adult sea urchin spine. Proc. Natl. Acad. Sci. U. S. A. *109*, 3699–3704. https://doi.org/10.1073/pnas.11092 43109.

Simonet Roda, M., Griesshaber, E., Ziegler, A., Rupp, U., Yin, X., Henkel, D., Häussermann, V., Laudien, J., Brand, U., Eisenhauer, A., et al. (2019). Calcite fibre formation in modern brachiopod shells. Sci. Rep. *9*, 598. https://doi.org/10.1038/s41598-018-36959-z.

Simonet Roda, M., Griesshaber, E., Angiolini, L., Rollion-Bard, C., Harper, E.M., Bitner, M.A., Milner, S., Ye, F., Henkel, D., Häussermann, V., et al. (2021). The architecture of Recent brachiopods - diversity of biocrystal and biopolymer assemblages in rhynchonellide, terebratulide, thecideide and craniide shells. Mar. Biol. https://doi.org/10.1007/s00227-021-03962-4.

Stevens, K., Griesshaber, E., Schmahl, W.W., Casella, L.A., Iba, Y., and Mutterlose, J. (2017). Belemnite biomineralization, development, and geochemistry: the complex rostrum of *Neohibolites minimus*. Palaeogeogr. Palaeoclimatol. Palaeoecol. *468*, 388–402. https://doi.org/10.1016/j.palaeo.2016.12.022.

Stolarski, J. (2003). Three-dimensional micro- and nanostructural characteristics of the scleractinian coral skeleton: a biocalcification proxy. Acta Palaeontol. Pol. *48*, 497–530.

Sun, X.D., and Holley, R.A. (2011). Factors influencing gel formation by myofibrillar proteins in muscle foods. Compr. Rev. Food Sci. Food Saf. *10*, 33–51. https://doi.org/10.1111/j.1541-4337.2010.00137.x.

Taylor, P.D., Lombardi, C., and Cocito, S. (2015). Biomineralization in bryozoans: present, past and future. Biol. Rev. *90*, 1118–1150. https://doi.org/10.1111/brv.12148.

Vinn, O. (2020). Biomineralization of polychaete annelids in the fossil record. Minerals *10*, 858. https://doi.org/10.3390/min10100858.

Von Neumann, J. (1952). Written discussion on a paper of C. S. Smith. In Metal Interfaces, C. Herring, ed. (American Society of Metals), pp. 108–110.

Wolfe, K., Smith, A.M., Trimby, P., and Byrne, M. (2012). Microstructure of the paper nautilus (*Argonauta nodosa*) shell and the novel application of electron backscatter diffraction (EBSD) to address effects of ocean acidification. Mar. Biol. *160*, 2271–2278. https://doi.org/10.1007/s00227-012-2032-4.

Wolfe, K., Smith, A.M., Trimby, P., and Byrne, M. (2013). Vulnerability of the paper nautilus (*Argonauta nodosa*) shell to a climate-change ocean: potential for extinction by dissolution. Biol. Bull. *223*, 236–244. https://doi.org/10.1086/BBLv223n2p236.

Woodward, S.P. (1880). Manual of the Mollusca, 4th Edition. (Crosby Lockwood and Co.).

WoRMS Editorial Board (2021). World register of marine species. http://www.marinespecies.org, at VLIZ.10.14284/170.

Xu, Y., Tijssen, K.C.H., Bomans, P.H.H., Akiva, A., Friedrich, H., Kentgens, A.P.M., and Sommerdijk, N.A.J.M. (2018). Microscopic structure of the polymer-induced liquid precursor for calcium carbonate. Nat. Commun. *9*, 2582. https://doi.org/10.1038/s41467-018-05006-w.

STAR★METHODS

KEY RESOURCES TABLE

REAGENT or RESOURCE	SOURCE	IDENTIFIER
Deposited data		
Mendeley Data	Mendeley Data	https://data.mendeley.com/datasets/n37bddwy7k/3
Experimental models: Organisms/strains		
Female *Argonauta hians* shells	Conchology Inc.	https://www.conchology.be/
Software and algorithms		
Corel Draw Graphics Suite (version Home & student X8)	CorelDRAW®	RRID:SCR_013674; http://www.coreldraw.com/us/
Image J	Schneider et al. (2012)	RRID:SCR_002285; https://imagej.nih.gov/ij/
AZtec	Oxford Instruments Nanoanalysis	https://nano.oxinst.com/products/aztec/
Channel 5 HKL, v. 4.3.	Oxford Instruments Nanoanalysis	https://nano.oxinst.com/products/aztec/aztechkl
TOPAS 5.0	Bruker AXS	https://www.bruker.com/en/products-and-solutions/diffractometers-and-scattering-systems/x-ray-diffractometers/diffrac-suite-software/diffrac-topas.html
SmartScan v.12	Park Systems	https://parksystems.com/products/operating-software/park-smartscan
XEI 4.3	Park Systems	https://parksystems.com/102-products/park-xe-bio
Dragonfly™ 4.1	Object Research Systems (ORS)	https://www.theobjects.com/company/products.html
Statistical Table Calculator	VassarStats	http://vassarstats.net/tabs_r.html

RESOURCE AVAILABILITY

Lead contact

Further information and requests for data should be directed to and will be provided by the Lead Contact, Antonio G. Checa (acheca@ugr.es).

Materials availability

This study did not generate new reagents or materials.

Data and code availability

The data can be obtained from the Lead Contact, Antonio G. Checa (acheca@ugr.es), or the coauthor Fátima Linares (flinaor@ugr.es).

Raw quantitative area measurements from Figures 5, 6, and S2, and raw crystallographic (EBSD) data (*.cpr and *crc files generated by AZtec software) from Figures 7 and S5 were deposited in Mendeley Data: https://data.mendeley.com/datasets/n37bddwy7k/3.

Any additional information required to reanalyze the data reported in this work paper is available from the Lead Contact upon request.

EXPERIMENTAL MODEL AND SUBJECT DETAILS

Shells

Four empty shells of *Argonauta hians* were purchased from Conchology Inc. (https://www.conchology.be/), two of which were used for analysis.. They all came from the Philippines (exact localities unknown). They are not protected by the Convention on International Trade in Endangered Species of Wild Fauna and Flora (CITES).

METHOD DETAILS

X-Ray diffraction (XRD)

Shell fragments were gently ground to a fine powder with an agate mortar and pestle and mixed with silicon powder (42.26 wt%). The mineralogy of the shell was analyzed with a Panalytical Xpert Pro X-ray powder diffractometer from the Department of Mineralogy of the University of Granada (UGR) (Cu Kα; 2Theta range: 4° to 120°; 0.013°step size; 100 s per step). To study the contribution of shell organic matrix to calcite lattice, the same sample was analyzed again after heating at 400°C and annealed for 30 mins. Calcite unit cell parameters and the percentage of amorphous were determined by Rietveld refinement using TOPAS 5.0 software (Bruker, Germany), considering calcite and silicon as the internal standard.

Thermogravimetry (TGA) and differential scanning calorimetry (DSC)

About 25 mg of powdered shell material were analyzed with a TGA and DSC coupled system from METTLER-TOLEDO (model TGA/DSC1) housed at the Center for Scientific Instrumentation (CIC) of the UGR. A heating rate of 10°C/min in air or nitrogen was used for registering the TGA/DSC scans.

Fourier-transform infrared spectroscopy (FTIR)

One shell fragment (~1 cm^2) was immersed in a decalcifying and etching solution (0.05M EDTA + 0.25 M HEPES + 2.5% Glutaraldehyde) until complete decalcification. The organic residue was washed with ultrapure distilled water (milli Q) and oven-dried. It was analyzed with an attenuated total reflection (ATR) diamond unit (ATR Pro One, Jasco) (Department of Mineralogy, UGR). The IR spectra were recorded at a 2 cm^{-1} resolution over 100 scans using a Fourier transform infrared (FTIR) spectrometer Jasco 6600. Four measurements were carried out in different areas of the membrane to obtain a coherent assertion (standard deviation and error) of the results.

Atomic force microscopy (AFM)

Analyses were done directly on both the outer and inner surfaces of shell fragments, previously cleaned with sodium lauryl sulphate. We used an AFM Park Systems NX20 (CIC, UGR) equipped with a cantilever ACTA (K= 40 N/m, F= 280 kHz) (CIC, UGR). Scans were done in tapping mode while displaying height, amplitude and phase signals. Images were obtained with Smart Scan v12 and subsequently analyzed with XEI 4.3 software (Park Systems).

Scanning electron microscopy (SEM)

Ultrasonicated fragments were cleaned by immersion in commercial bleach (~5% active chlorine) for 10 min. Successive washings in MilliQ ultrapure water, for 2-3 min each, followed. Dried fragments were embedded in epoxy resin (EpoFix, Struers), sanded, and polished in successive steps until a mirror–like polish was obtained with 0.25 μm diamond suspension (Struers). Some of the polished samples were etched (2.5% glutaraldehyde, 0.25M HEPES buffer, and 0.05M EDTA), for 2 min in an orbital shaker. Other samples were exposed to the etching/fixing solution for much longer times to completely denudate the organic network. All samples were carbon-coated (Emitech K975X carbon evaporator) and observed in the field emission SEMs (FESEMs) Zeiss Auriga and FEI QemScan 650 F (CIC, UGR).

Electron backscatter diffraction (EBSD)

Shell samples were embedded in epoxy resin and subjected to several sequential grinding and polishing steps. The two final steps consisted of etch-polishing with colloidal alumina in a vibratory polisher and subsequent polishing with an Ar beam in an ion polisher. The samples were coated with 4-6 nm of carbon. Measurements were carried out on a Hitachi SU5000 field emission SEM, equipped with an Oxford EBSD detector (DEES, LMU). The SEM was operated at 20 kV. Data acquisition (with step sizes of 150 and 300 nm) was done with the Aztec (Oxford Instruments) software.

Information obtained from EBSD measurements is presented as grey-scaled band contrast measurement images and as color-coded crystal orientation maps with corresponding pole figures; the latter giving either individual data points or contours. In the latter case, we use the lowest possible degree for half-width (5°) and cluster size (3°). The half-width controls the extent of the spread of the poles over the surface of the project sphere. A cluster (or domain) comprises data with the same orientation. The color code used for crystal orientation is either given in the figure or stated in the figure caption. EBSD band contrast gives the signal strength of the EBSD-Kikuchi diffraction pattern at each measurement point and is shown as a

grey-scale component in a map. When the strength of the EBSD signal is high, we find bright gray colors in the map, whereas when it is weak or absent, gray colors are dark. Crystal co-orientation statistics are derived from density distributions in pole figures and are given as MUD (multiple of uniform distribution) values. The higher the MUD, the higher the co-orientation. All post-processing was done with the Oxford Instruments CHANNEL 5 HKL software.

3D reconstruction by focused ion beam coupled to SEM (FIB-SEM)

Three volumes were reconstructed by using the slice and view technique by means of FIB-SEM. Two of them were scanned with a TESCAN Amber X FESEM equipped with Plasma FIB (TESCAN Central Demo Lab & Applications, Brno, Czech Republic). Polishing was done using a current of 10 nA, and a rocking stage was used to reduce the curtaining effect. Images were acquired in backscatter electron (BSE) mode at 5 kV. The first scanned volume (TESScan 1), with dimensions (width x height x depth) 25x30x29 μm, consisted of 182 slices with a thickness of 50 nm, oblique to the growth direction of the fibers. The second volume (TESScan 2) (50.5x32.4x31.9 μm) consisted of 525 slices perpendicular to the growth direction; slice thickness was 60 nm. A third volume (ZEISScan 1) was analyzed with a Zeiss Crossbeam 350 FESEM, equipped with a gallium FIB column (Carl Zeiss Microscopy GmbH, Oberkochen, Germany). The polishing current was 50 pA. Images were collected in Energy Selective Backscattered (EsB) mode. The volume scanned (12x12x3.6 μm) generated 360 images perpendicular to the growth direction, separated by a thickness of 10 nm.

Area analyses were done with FIJI software (Image J). Raw TIFF images were converted to 8-bit images. After B/W threshold adjustment, we applied Noise-Despeckle followed by Binary-Watershed. Before particle analysis, polygon boundaries of TESScan 1 and ZEISScan 1 images were manually retouched for maximal accuracy. Given the high number of polygons (thousands) contained within the images of TESScan 2, we skipped this procedure. Video, segmentations and 3D meshes were done with Dragonfly™ 4.1 software after slice registration (registration method SSD). All the procedures were carried out at the CIC (UGR).

Transmission electron microscopy (TEM)

The surface of a shell fragment was scraped with a scalpel. Fragments were ground in an agate mortar and the powder was suspended and sonicated in pure ethanol. The solution was dropped onto lacy carbon copper grids and air-dried for subsequent TEM observation. Measurements were acquired using a double Cs corrected FEI Titan G2 60-300 TEM equipped with an X-field emission gun and a Gatan Ultrascan camera (CIC, UGR). Imaging was performed in TEM mode at 300 kV, and 0.5-1 s exposure. Nanodomains were indexed by Fast Fourier Transform (FFT) analysis.

Other shell fragments, were immersed in a fixing decalcifying solution (0.05 M EDTA, 2.5% glutaraldehyde, and 0.25M HEPES) until complete decalcification occurred (48-72 h). The residual membranes were critical-point dried (Leica EM CPD300), post-fixed in OsO4 (2%) for 2 h at 4°C and embedded in epoxy resin Epon 812 (Electron Microscopy Science, EMS). Ultra-thin sections (50 nm), obtained with an ultramicrotome Leica Ultracut R, were stained with uranyl acetate (1%), followed by lead citrate. They were later carbon-coated and observed with TEM Zeiss Libra 120Plus (CIC, UGR).

Illustration

All figures were illustrated by using the Corel Draw Graphics Suite (version Home & Student X8).

Video production

Video production for TESScan 1, TESScan 2, and ZEISScan 1 datasets (see subsection "3D reconstruction by focused ion beam coupled to SEM (FIB-SEM)" above for details) was performed with Dragonfly 4.1 Movie Maker. Only the video generated from ZEISScan 1 dataset is presented, as Video S1.

QUANTIFICATION AND STATISTICAL ANALYSIS

Statistical analyses were made with Statistical Table Calculator (http://vassarstats.net/tabs_r.html).